ELSEVIER

3D image-based characterization of fluid displacement in a Berea core

M. Prodanović [a,*], W.B. Lindquist [b], R.S. Seright [c]

[a] *Institute for Computational and Engineering Science, University of Texas at Austin, 1 University Station, C0200, Austin, TX 78712, USA*
[b] *Department of Applied Mathematics and Statistics, Stony Brook University, Stony Brook, NY 11794-3600, USA*
[c] *New Mexico Petroleum Recovery Research Center, New Mexico Institute of Mining and Technology, 801 Leroy Place, Socorro, NM 87801, USA*

Abstract

Improved network flow models require the incorporation of increasingly accurate geometrical characterization of the microscale pore structure as well as greater information on fluid–fluid interaction (interfaces) at pore scales. We report on three dimensional (3D) pore scale medium characterization, absolute permeability computations for throat structures, and pore scale residual fluid distribution in a Berea core. X-ray computed microtomography combined with X-ray attenuating dopants is used to obtain 3D images of the pore network and to resolve phase distributions in the pore space.

We present results on pore characterization, including distributions for pore volume, pore surface area, throat surface area, and principal direction diameters for pores and throats. Lattice Boltzmann computations are used to predict absolute permeabilities for individual throats reconstructed from the images. We present results on oil and water distribution in the pore space at residual conditions. We also consider the effects on residual fluid distribution due to the injection and gelation of a water-based gel. In extensive studies of Berea cores it has been observed that introducing water-based gels in the displacement process reduces permeability to water more than to oil. Our results provide supporting evidence for the involvement of gel compaction (dehydration) and oil trapping, while discounting gel blockage in throats, as mechanisms contributing to this effect.
© 2006 Elsevier Ltd. All rights reserved.

Keywords: Porous media; Berea; Pore scale characterization; Permeability; Network flow; Lattice Boltzmann; Residual saturation; Gels

1. Introduction

Quantification of microscale porous medium parameters and the relationships between them is of utmost importance in the prediction of macroscale fluid flow properties. Lattice Boltzmann (LB) (e.g. [44,22,29,38]) or network flow (NF) (see e.g. [4,5] for reviews) model computations provide the major computational tools for relating microscale parameter relationships to bulk flow properties. Given limitations of current computer technology, network flow calculations can model substantially larger effective volumes, though at a loss of medium resolution, as only a selected subset of medium properties is considered in a network model. We note that predictive modeling of bulk flow properties will require computation over an ensemble of stochastically equivalent network models to establish both predictive means as well as expected variance in flow behavior [14,39,41,42].

Since the late 1980s, X-ray computed microtomography (XCMT) [10] has provided a tool for the non-destructive investigation of the 3D microstructure of porous materials. The analysis of the geometric structure of porous media [13,15,31,40,41] as captured in 3D XCMT images and other imaging modalities provides improved geometric parameter characterization useful for input to LB and NF models. We have been actively involved in developing numerical, image analysis tools to extract quantitative information on the stochastic nature of the microstructure of sandstones [16–20,37]. Since the late 1990s, the introduction of X-ray absorbent dopants to provide contrast between fluids has enabled non-destructive XCMT studies [35,36,46] of the 3D distribution of fluids in the pores. This

* Corresponding author. Tel.: +1 512 2327767; fax: +1 512 4718694.
E-mail addresses: masha@ices.utexas.edu (M. Prodanović), lindquis@ams.sunysb.edu (W.B. Lindquist), randy@prrc.nmt.edu (R.S. Seright).

has the potential to replace micromodel flow studies [24], where the network is dominated by two dimensional effects. The analysis of 3D fluid distribution in the pore network provides input to, as well as validation tests for, LB and NF modeling that is only beginning to be explored.

Fig. 1 sketches our view of one potential interplay between the experimental input and validation data provided by XCMT. In this view, geometrical analysis of XCMT images provides information on geometrical properties (and relationships between them) that are used as input to NF models. This geometric input is either in the form of the actual imaged network or in terms of geometrically equivalent (in a stochastic sense) networks.

The fluid characterization data obtained from XCMT can also be used as input. For example, computation of fluid–fluid interfacial area can be used to obtain parameters for constitutive relationships among interfacial area, saturation, capillary pressure and resistance terms presented in recent theoretical two-phase flow models [27,32]. In addition, the fluid characterization data can be used to validate NF output, for example in a "history-matching" mode to tune parameters involving poorly known relationships in order to obtain an improved match between NF output and XCMT fluid data.

In this paper we concentrate on three aspects of the scheme outlined in Fig. 1. First, we discuss the geometrical pore scale characterization obtainable from XCMT. In addition to distributions of pore volume, throat area and coordination number (measurements of which, in various forms, have been generated for some time now), we present distributions for (i) surface areas of individual pores, (ii) pore diameter length in each of the principal directions computed for each pore, (iii) a newly defined pore shape factor.

Second, while throat and pore conductivities for NF models are universally produced from analytic models based upon geometrically simplified shapes (typically assuming axial or spherical symmetry), we demonstrate how LB models can be used to provide more realistic absolute permeability values, based on exact (to the resolution of the image) throat (and, by analogous computation, pore body) configurations for input to NF models. Such permeabilities can also be used in stochastic network models by correlating the computed permeability with a geometrical parameter of the throat geometry (e.g. throat area).

Third, we demonstrate capability for XCMT-based characterization of fluids in the pore space. As demonstrated by our discussion, this not only has the potential to contribute to improved NF modeling, but can lead to an understanding of fluid competition mechanisms at the pore level, paralleling the type of scientific result obtainable from glass micromodels. Thus in addition to presenting improved results [35,36] on the pore-scale partitioning of oil and water in Berea sandstone at residual fluid conditions, we consider, and propose a mechanism for, fluid re-partitioning effects and permeability changes due to the addition of an aqueous-based gel into the pore space. While this is a problem specific to petroleum engineering, the framework of the analysis is far more general and can be applied to any time sequence of fluid displacement images of the same region.

As a brief introduction to this problem we note that the amount of (contaminated) water produced in oil production wells is on average three times that of oil, and therefore poses considerable environmental threat. The filling of local pore space with an aqueous-based polymeric gel is the most common chemical field treatment of oil production wells to control water production. Gel treatment can reduce permeability to subsequent water flow by a factor of 10^4 [34] compared with single phase permeability to water in the absence of gel. Gel placement in two phase flow situations causes analogous, though disproportionate, phase permeability reductions. This disproportionality is quantified in terms of the residual resistance factor to oil, F_{rro}, defined as the ratio of relative permeability to oil flow at residual water conditions before and after gel placement, and the residual resistance factor to water, F_{rrw}, defined as the ratio of relative permeability to water flow at residual oil conditions before and after gel placement. In Berea cores, $F_{rro} \approx 10$ while $F_{rrw} \approx 10^3$. During oil field treatments when, for example, production wells are treated with gelants, some zones have high water saturation and high fractional water flow and other zones have high hydrocarbon saturation and fractional flow. After gel placement, in the oil zones, oil is the first fluid to flow through gel zones and F_{rro} and the mechanism determining its values are field-relevant. In water zones, water is the first fluid through gel zones and the permeability reduction factor of $\approx 10^4$ for water through aqueous gel is relevant. However, active management of fields, with the potential for long term, induced changes in flow patterns make the study of the disproportionate value for F_{rrw} of scientific interest as well.

2. Experimental procedure

Our results for this paper are based upon analysis of a single Berea sandstone core, as a partial demonstration of the amount of useful data that can be extracted from one core.
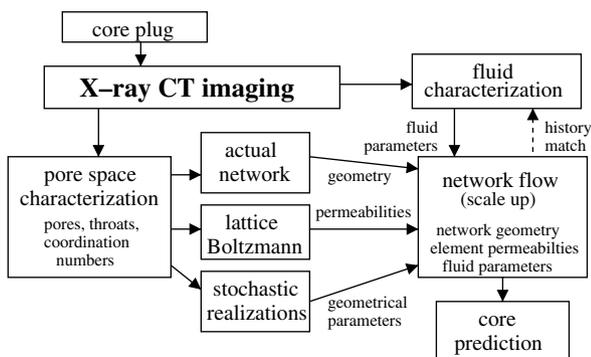

Fig. 1. A sketch of our view of the inter-relationships between XCMT, LB and NF models for improved prediction of fluid flow at core scales.

A 6.5 mm diameter, 35 mm length core was prepared from a larger Berea sample having bulk absolute permeability 0.464 μm^2 (0.47 Darcy) and experimentally measured bulk porosity of 22%. Specific measurements of grain size were not made on this sample, however the grain size in Berea sandstone is typically reported to be in the range 0.2–0.25 mm. The core was saturated with brine containing 1% NaCl and 0.1% $CaCl_2$ and imaged at the tomographic facility on the X2B beam line [9] at the National Synchrotron Light Source at Brookhaven National Laboratory. Beam energy was 33.3 keV. A 2.52 mm long section centrally located along the length of the cylindrical core was imaged at 4.93 μm voxel resolution. Using the experimental setup described in [36], the core was successively imaged at residual fluid conditions occurring during a sequence of floods. The experimental apparatus enabled the sequence of fluid injections to be performed without removing the core from the mounting stage.

The fluid injection sequence was: 35 pore volumes (PV) of oil; 70 PV of brine; 10 PV of aqueous gel; 20 PV of oil; 2.5 PV of brine. Fluid was injected with a pressure gradient of 117.2 kPa across the length of the core. After gel injection, but before imaging, the core was heated to ~60 °C for 12 h to effect gelation. The aqueous gel was Cr(III)-acetate–HPAM (hydrolyzed poly-acrylamide) consisting of (by weight) 0.5% Alcoflood 935 HPAM, 0.0417% Cr(III) acetate, 1% NaCl, and 0.1% $CaCl_2$. The oil was hexadecane doped with 10% (by weight) iodohexadecane. All experiments were performed at room temperature except during gelation. Fluid viscosities were: brine – 10^{-3} kg/m s (1 cP), hexadecane – 3.3×10^{-3} kg/m s, gel – 20×10^{-3} kg/m s.

These fluids produce no significant chemical reactions that would affect the core pore space. The hexadecane is inert. The polymer is inert at room temperature though it reacts with the chromium cross-linker at the elevated gelation temperature. NaCl (1%) and $CaCl_2$ (0.1%) in the brine inhibit any swelling of clays present in core; the $CaCl_2$ will also inhibit any dissolution of carbonate minerals in the rock. A very small quantity of chromium may be taken up by the clays when the gelant is injected into the core, but the amount would have no significant effect on the pore space.

Permeability measurements were recorded as a function of pore volume injected during each injection sequence. Permeabilities used to compute F_{rro} and F_{rrw} were taken at the end of the sequence when residual conditions had been established. At the end of each injection stage, flow was halted (release of pressure gradient) while tomographic imaging was performed. After each 3D image was acquired, the core was rotated to zero position to ensure not only that the same region was re-imaged after each flood but also to ensure voxel alignment between images.

From each image, a common $450 \times 450 \times 475$ voxel (11.5 mm^3) rectangular region was subjected to image analysis. The size of the analyzed volume was determined by limitations of the 1 GByte of memory on the single processor hardware used for the image analysis. For purposes of reference, the sequence of images will be identified as s_w (brine saturated core), s_{wr} (residual brine after oil flood), s_{or} (residual oil after brine flood), gel (post-gel injection), $gels_{wr}$ (residual brine post-gel injection), and $gels_{or}$ (residual oil post-gel injection).

3. Image analysis

Using the software package 3DMA-Rock [1,17,18,20], the images were analyzed for pore structure and fluid distribution. The addition of iodohexadecane to the oil phase improves the X-ray attenuation contrast between the brine and oil phases, but at the cost of blurring the contrast between the oil and rock phases. Consequently the location of the rock phase is determined solely from the s_w image; rock location in subsequent images in the sequence is then inferred from its location in s_w. We utilize a segmentation algorithm based on indicator kriging [28] to determine the interface between rock-brine (s_w image) and iodohecadexane-brine (subsequent images). The partition into a network of pores and throats is performed on the s_w image as described in [18]. It is important to note that our division of the pore space is into pores separated by throat surfaces and is *not* a division into pores separated by channels. (We know of no geometrical measure to decide where a pore stops and a connecting channel begins in real rock void space.) Thus the *entire* volume of the pore space is divided into pores.

An important aspect of our image analysis is the ability to identify and reconstruct individual throats in the pore space [17,18]. Briefly, the medial axis transform of the pore space provides a geometrically faithful network of linked paths used to search the pore space. A subset of these paths are in one-to-one correspondence with the physical pathways linking separate pore bodies. We have constructed algorithms to search each such path and find the minimal cross-sectional (i.e. the throat) surface along the path. Fig. 2(a) shows one such (digitized) path and the triangulated throat surface found. Note that we maintain no restriction that the throat surface lie in a single plane. Fig. 2(a) also shows the path and throat surface relative to the surrounding grain surface. The surface is represented here as a smoothed triangulated surface by means of the marching cubes algorithm [3,21].

Our ability to determine distributions for pore volume/effective radius, throat area/effective radius, coordination number and pair-wise correlations between these geometrical parameters has been described elsewhere [17,18]. We have recently added the abilities to compute principal diameters and a shape factor for pores in order to obtain quantitative measures which would allow non-sphere approximations to pore shapes. We have also developed the computation of surface areas for individual pores. We present results from these new capabilities here.

The center-of-mass location and the three principal directions are determined for each pore using a moment-of-inertia analysis. Thus the principal directions always
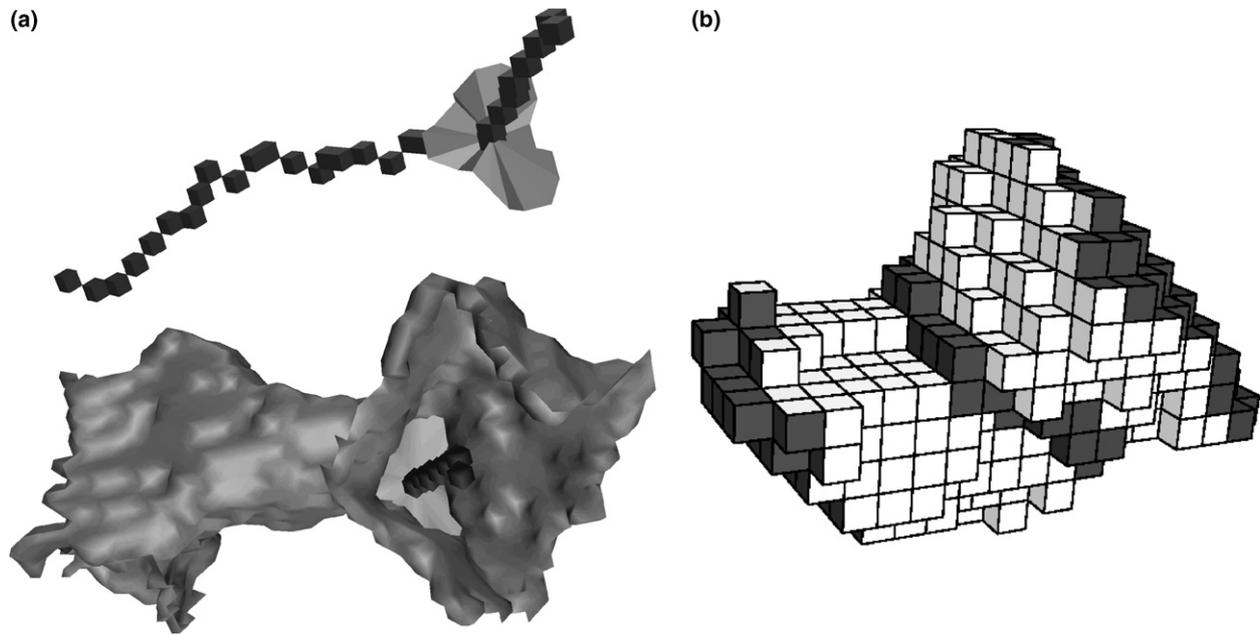
Fig. 2. (a) (Top) A medial axis path showing the computed throat surface. (Bottom) As in the top with a triangulated rendering of the channel surface in the vicinity of this throat. (b) A digitized rendering of the pore voxels within a distance of 6 voxels on each side of this throat surface. Appropriate faces of those voxels for which inlet and outlet boundary conditions for the LB computations are to be applied, as well as those voxels through which the throat surface passes, have been shaded dark gray. For clarity of presentation, grain voxels are not displayed.

form an orthogonal basis local to each pore. Three principal diameters are determined for each pore by measuring the pore width through the center of mass along each of the principal directions. The diameters are labeled D_1, D_2 and D_3 in decreasing length.

Mason and Morrow's [23] analysis of the relationship between drainage and imbibition capillary pressure and arc meniscus radius in capillary tube cross-sections introduced a cross-sectional shape factor $G \equiv A/P^2$, where A and P are cross-sectional area and perimeter respectively. G is a dimensionless quantity arising naturally in the relationship between the (dimensionless) radius of the arc meniscus, the fluid wetting angle, and the vertex angles of a triangular capillary. This concept has subsequently been employed (e.g. [30,43]) in network flow models employing effective triangle or quadrilateral cross-section pores and throats. While shape factors for a 3D pore might be defined by averaging shape factors over 2D cross-sections of the pore, as pore geometry is usually extremely irregular, individual 2D cross-sections (for a single pore) may often consist of two or more disconnected components, leading to ill-defined shape factors. We therefore propose a fully 3D shape factor, $G_{3D} \equiv V/S^{1.5}$, where V and S are respectively pore volume and surface area. This definition is motivated in order to capture deviation from spherical shapes; under this definition, a sphere has a constant shape factor of $(6\sqrt{\pi})^{-1} \approx 0.094$, while, for example, the shape factor for a cylinder scales as $\sqrt{t}$, where $t \equiv r/l$ is the length-normalized radius of the cylinder.

As counting voxel faces [2] can lead to large errors in surface area computation, we utilize the marching cubes algorithm [3,21] which provides a more reliable [8] triangulated surface from which to measure area. Pore surface areas are computed by "sealing" each throat opening with a (6-connected) set of voxels. This set consists of those voxels that are cut by the triangulated throat surface. The surface area of each pore is therefore the area of the triangulated interface which separates the void space of the pore from the rock/throat voxels sealing that pore.

For the LB-based computation of absolute (single phase) throat permeabilities, the throats in a 256^3 voxel subvolume of the s_w image were considered. For incompressible fluid flow, the throat constriction controls the flow through that pathway. Thus in order to compute absolute permeability, there is no need to simulate pore space along the full length of the pathway. We therefore reconstruct the (digitized) channel shape enclosing the pathway to a distance of six voxels on each side of throat region voxels using a 6-connected grassfire algorithm. Relevant pore voxels in the reconstructed channel segment are identified as inlet, outlet, and grain boundary voxels. A 6-connected grassfire is preferred in this instance (over a 26-connected one) since the inlet/outlet edges of the reconstructed region remain parallel to the throat surface (which is not usually aligned with the digitization axes). The choice of a reconstruction distance of six voxels up- and downstream of the throat to define the channel segment for the absolute permeability computation is a compromise between speed of the LB computation, accuracy in capturing the channel geometry local to the throat, and maintenance of roughly parallel inlet/outlet boundaries. (For more discussion on this latter point, see Section 4.) Fig. 2(b) shows a digitized view of the pore voxels in the channel within a six voxel distance on each side of the

throat. Dark shaded voxels identify those cut by the throat surface as well as voxels that play the role of inlet and outlet nodes for the LC computation. A normal vector to the throat surface is computed from the tangential direction to the medial axis as it passes through the throat surface. This normal direction is used to determine the direction of an applied pressure gradient to simulate flow through the throat geometry. The direction of the pressure gradient distinguishes the inlet end of the channel from the outlet.

In images s_{wr} through gels$_{or}$, the rock matrix is identified from the analysis of s_w. The fluid filled space is then subjected to binary segmentation using the kriging-based segmentation algorithm [28] to identify the oil and brine phases (the water-based gel is indistinguishable from brine phase). In addition to determining oil and brine saturations for the entire image, by inserting the throat surfaces determined in s_w into the pore space of the rest of the images, saturations can be determined on a pore-by-pore basis.

Each fluid phase is separately analyzed. We characterize the connectivity of each fluid phase by computing the number, location and size of the individual disconnected "blobs" of each phase. In computing connectivities of the two fluid phases, it is important to retain a 6-connected, 26-connected distinction between the two phases. We treat the wetting phase as 26-connected (the brine phase in the case of Berea) and the non-wetting phase (hexadecane) as 6-connected. We are also interested in the "pore occupancy" of each phase [6], where the pore occupancy of a blob is defined as the number of pores it spans.

4. Lattice Boltzmann computations

Throat permeabilities were computed using the single phase, 3D lattice Boltzmann model

$$f_i(\vec{x} + \vec{e}_i \Delta t, t + \Delta t) - f_i(\vec{x}, t)$$
$$= -\frac{1}{\tau}[f_i(\vec{x}, t) - f_i^{eq}(\rho(\vec{x}, t), \vec{u}(\vec{x}, \rho, t))] - 3\frac{w_i}{c^2}\Delta t \vec{e}_i \cdot \nabla p. \tag{1}$$

Our notation is standard [7,38].

The first term on the RHS is the Bhatnagar–Gross–Krook (BGK) single relaxation time scale collision term. The equilibrium distribution function is

$$f_i^{eq}(\rho, \vec{u}) = \rho w_i \left[1 + \frac{3}{c^2} \vec{e}_i \cdot \vec{u} + \frac{9}{c^4}(\vec{e}_i \cdot \vec{u})^2 - \frac{3}{2c^2} \vec{u} \cdot \vec{u} \right]. \tag{2}$$

We employ the 3D 19 velocity model D3Q19 [11]; thus $i = 0, \dots, 18$. The values for the weights w_i are 1/3 for the $(0, 0, 0)$ direction, 1/18 for the $(1, 0, 0)$ (and similar) directions, and 1/36 for the $(1, 1, 0)$ (and similar) directions.

The second term on the RHS of (1) is a body force term used in a standard way to model an externally imposed pressure gradient ∇p [44]. As discussed in Section 3, the direction of the applied pressure gradient is perpendicular to the throat surface.

As we are interested in permeability at steady state flow conditions, the initial distribution fluid probability densities, $f_i(\vec{x}, t)$, were set using equilibrium values (2) for a constant density fluid at rest. Steady state conditions were assumed reached when the error in the relative velocity at each computational node obeys

$$\frac{\|\vec{u}(x, t + \Delta t) - \vec{u}(x, t)\|_2}{\|\vec{u}(x, t)\|_2} < \epsilon. \tag{3}$$

A value of $\epsilon = 10^{-6}$ was used.

No-slip boundary conditions are used for the pore-grain surface. We used the curved boundary conditions of [25,26] which provided improved convergence to steady state flow conditions compared to standard bounce-back boundary conditions.

Inlet/outlet boundary conditions are somewhat problematic. If inlet/outlet faces are planar then Dirichlet conditions for pressure can be maintained as boundary conditions [11]. As exemplified in Fig. 2(b), our inlet and outlet boundaries may curve. (As mentioned, the use of a 6-connected grassfire to define the set of pore voxels in the LB computation minimizes such curvature). The irregular nature of the pore geometry makes it difficult to amend our inlet/outlet boundaries to planar structure. We have therefore reverted to the body force term in (1) to implement the pressure gradient. Let $\hat{n}$ denote the unit vector in the direction of the pressure gradient. We therefore require $\partial \vec{u} / \partial \hat{n} = 0$ at the inlet/outlet boundaries. We argue that this is a fairly reasonable boundary condition to impose.[1] Implementation of this boundary condition is achieved by copying values of appropriate f_i across the boundary. For planar boundaries, this provides a second order accurate implementation for this boundary condition. When boundaries curve, obvious approximations to this rule are invoked. In extreme cases, the default condition is to utilize an equilibrium value f_i^{eq} corresponding to the current velocity to fill missing values at a boundary point.

Throat permeability is computed from Darcy's law

$$Q/A = -(K/\mu)\nabla p, \tag{4}$$

where Q denotes the volumetric flow rate, A is the normal cross-sectional area of the flow, and $\mu = \nu\rho$ is dynamic fluid viscosity; ν is its kinematic viscosity. We compute the volumetric flow rate Q at steady state conditions through a plane passing through the center of the throat. As the throat may be at arbitrary angle to the lattice, we utilize that coordinate system plane (xy, yz, zx) that is closest to being perpendicular to the throat. The desired flux Q is, of course, the component of the flux normal to the plane selected.

---

[1] We note that use of the 6-connected grassfire to define the computational volume in the pore space surrounding the throat surface (i.e. to locate the inlet/outlet surfaces) means that most of the time $\hat{n}$ is in fact normal to the inlet/outlet surface. Thus over most of the inlet/outlet surface, our inlet/outlet boundary condition is a zero-Neumann condition on the normal velocity across the surface.

The LB was validated on Hagen–Poiselle flow simulations (flow down cylinders of constant cross-sectional area). The parabolic radial velocity profiles obtained were in good agreement with analytic values. For the validation runs, the inlet/outlet boundaries were planar surfaces normal to the cylinder axis.

5. Results

Fig. 3(a) shows a small region of a slice from the image stack acquired when the pore space was brine saturated. In addition to the visible pore space and sandstone grains, there appear highly attenuating impurities (e.g. feldspar) in the rock matrix, as well as the suggestion of some clay in the pore space. In our analysis the clay filled regions are treated as grain. Fig. 3(b) shows the same region in the s_{or} (residual oil) image. Hexadecane occupancy in areas of the pore space is clearly visible. Fig. 3(c) is a composite picture showing the pore/rock segmentation resulting from Fig. 3(a) superimposed on the brine/hydrocarbon segmentation resulting from Fig. 3(b).

5.1. Pore space characterization

Analysis of s_w gives a porosity of 18% for the imaged subregion of the Berea sample. (We note that this finding

does not contradict the overall 22% porosity measured for the bulk sample from which this core was taken. Heterogeneity in the porosity distribution of the bulk sandstone sample is visually evident. The cutoff length scale for spatial correlation in the porosity distribution in Berea has been estimated to be around 3 mm [14].) The pore volume distribution determined from s_w is shown in Fig. 4. Paralleling the results of our analysis on Fontainebleau sandstone cores [18,19], the pore volume distribution is seen to be log-normal, with mean pore volume 6.2×10^{-4} mm^3.

The distributions determined for pore diameters D_i, $i = 1, 2, 3$ and effective radius R_{eff} (radius of sphere of equivalent volume) and are displayed in Fig. 4. Interestingly, the distribution of the smallest pore *diameter* D_3 and that for the equivalent sphere *radius* R_{eff} are strikingly similar. We have also computed the pore diameters along the x-, y- and z-directions through the center of mass. These directions should be arbitrarily oriented with respect to the pore principal directions (assuming pore isotropy) and should produce distributions similar to each other and (given the pore anisotropy seen in $D_1 \rightarrow D_3$) different from the $D_1 \rightarrow D_3$ distributions. The distribution D_x for diameters measured in the x-direction is also displayed in Fig. 4. The D_y and D_z distributions are virtually identical to D_x, even to the elevated density occurring over the diameter range 70–75 µm. This elevated density corresponds to
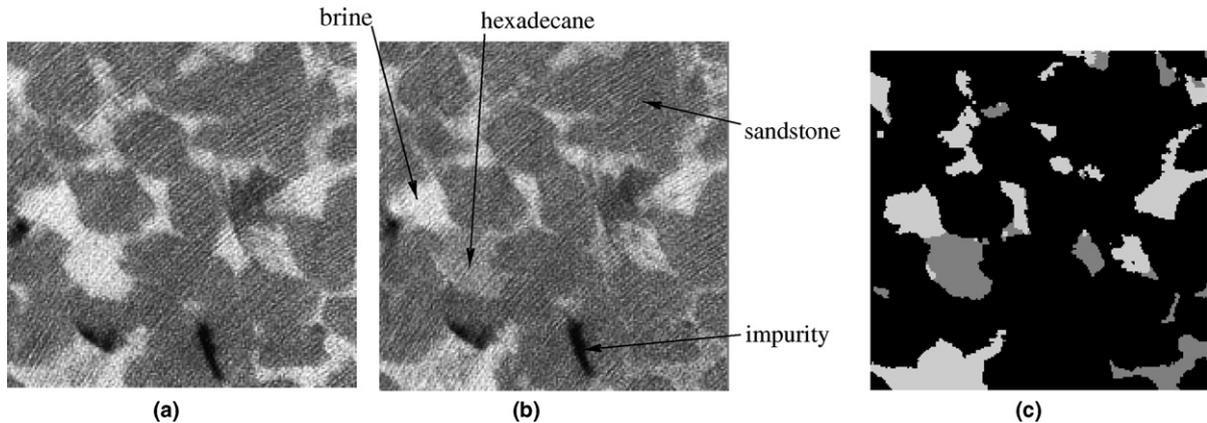

Fig. 3. (a) A subregion in s_w. (b) The same region in s_{or}. (c) Pore/rock and brine/oil segmentation results for this region.
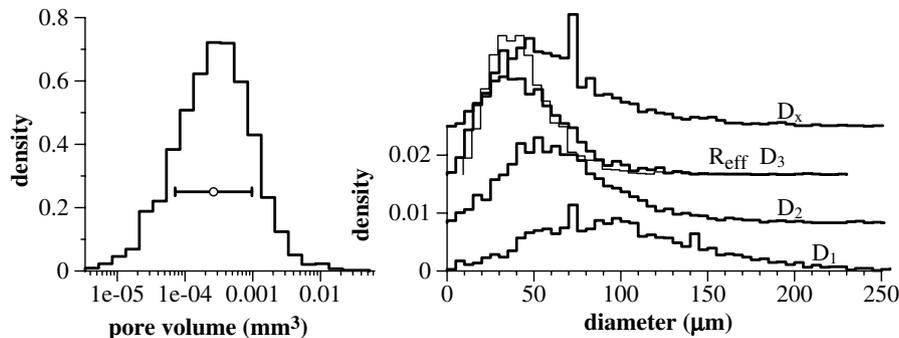

Fig. 4. (Left) Pore volume and (right) pore diameter distributions determined from s_w. (Left) The open circle and horizontal bar indicate mean and standard deviation of the distribution. (Right) All plots are to the same vertical scale, but D_1, D_2, D_3 and D_x, have been vertically displaced from each other for visual clarity. R_{eff} (light curve) is drawn with the same vertical displacement as D_3 to demonstrate the similarity between the two plots.
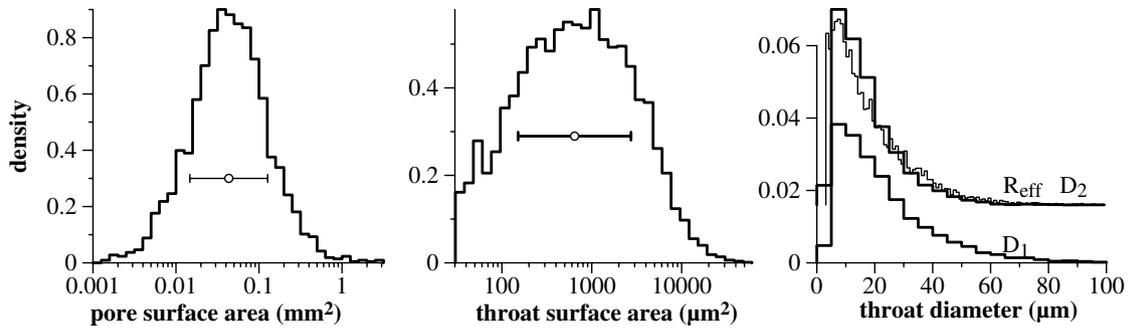
Fig. 5. (Left) Pore surface area, (middle) throat surface area and (right) throat diameter distributions determined from s_w. (Left, middle) The open circle and horizontal bar indicate mean and standard deviation of the distribution. (Right) All plots are to the same vertical scale, but D_1 and D_2, have been vertically displaced from each other for visual clarity. R_{eff} (light curve) is drawn with the same vertical displacement as D_2 to emphasize the similarity between the two plots.

the peak in the D_1 distribution and presumably occurs whenever the largest principal axis direction of a pore aligns with one of the x-, y- or z-directions.

Pore and throat surface area distributions determined from s_w are shown in Fig. 5. The pore surface area distribution also appears to be log-normal, with mean value corresponding to a surface area of 0.043 mm². Note the surface area of a pore in this plot includes the surface area of its throats. As for pores, diameters along the two principal directions were determined for each throat surface, as well as an effective radius determined from the circle of equivalent area. The diameters are labeled D_1 and D_2 in decreasing length. The distributions determined for D_1, D_2 and R_{eff} are displayed in Fig. 5. Analogous to pores, the distribution of the smallest throat *diameter* D_2 and the equivalent circle *radius* R_{eff} are strikingly similar. The effect of voxel resolution is clearly seen as a sharp cut-off at the left side of both the throat surface area and diameter distributions.

Fig. 6 shows the distribution of shape factors obtained from the Berea core analyzed in this study. The shape factor appears to be normally distributed, with mean and standard deviation values of $(3.7 \pm 1.2) \times 10^{-4}$. Fig. 6 also shows the correlation between shape factor and pore volume. The shape factor decreases with volume, as larger pores have, in general, a more complicated surface. The shape factor values quantify the decidedly non-spherical

nature of individual pores in Berea sandstone. We also note, but do not show here, that the shape factor dependence is not consistent with an assumption of cylindrically shaped pores.

5.2. Throat permeabilities

We model water as the simulated fluid. Eq. (1) was computed in dimensionless form using a reference length, time increment and mass. The reference length, $\Delta x = 4.93$ μm, was given by the grid spacing of the digitized image. The reference time was determined from the sound speed relation $c_s = c/\sqrt{3}$, where c_s is the sound speed for the Navier–Stokes equations to which this LB converges and $c = \Delta x/\Delta t$ is referred to as the lattice speed. Using a sound speed for water of 1482 m/s (room temperature, standard pressure) and the reference length, gives a reference time increment of 1.92×10^{-9} s. A reference mass of 1.198×10^{-13} kg was chosen to ensure that the dimensionless density of the resting fluid is 1.0.

With a reference length of 4.93 μm, we estimate a Knudsen number of approximately 10^{-2}, validating the assumption that the LB is approximating Navier–Stokes flow.

τ and the kinematic fluid viscosity are related by

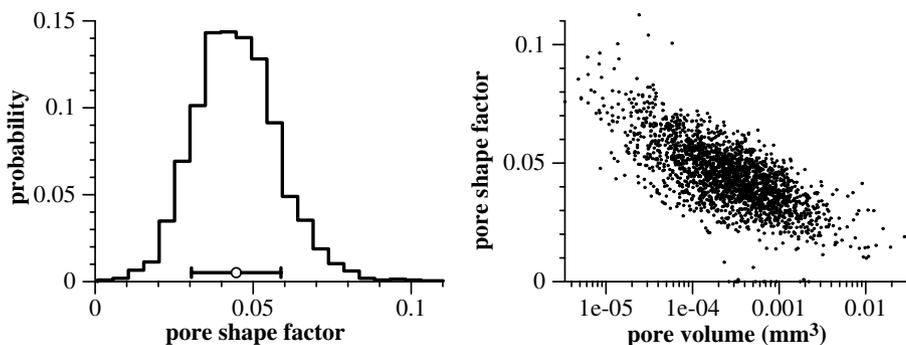$$v = (2\tau - 1)c^2\Delta t/6. \tag{5}$$

Fig. 6. (Left) Pore shape factor. The open circle and horizontal bar indicate mean and standard deviation of the distribution. (Right) Pore shape factor correlated with the pore volume. According to our definition, pore shape factor of a ball is 0.0531. The general trend of bigger pores having smaller pore shape factor leads to conclusion that bigger pores have in general more complicated, rugged surface.
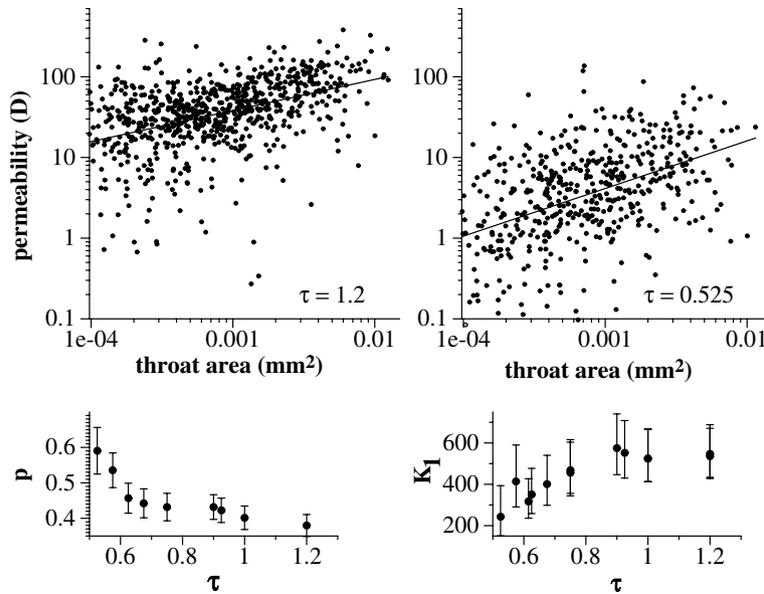
Fig. 7. (Top) LB computed throat permeabilities correlated with throat area for two values of the relaxation parameter. The straight line in each represents a least square fit. (Bottom) Dependence of the fit parameters p and K_1 on the relaxation parameter.

The kinematic viscosity of water at standard conditions is 10^{-6} m^2/s, requiring a value of $\tau = 0.500237$, just above the restriction $\tau > 0.5$ needed for positivity of v. We were unable to achieve convergence in the computations below $\tau = 0.525$. We therefore computed with τ in the range $[0.525, 1.2]$, giving effective kinematic viscosity for the "water" in our computations in the range $[1 \times 10^{-4}, 3 \times 10^{-3}]$.

We prescribed a pressure gradient of 3.35×10^6 Pa/m, which matches, on average, that produced by the 117.2 kPa pressure drop applied across the 35 mm core in the experimental fluid flows on this core.

For each individual throat, only a few thousand iterations were needed to reach steady state conditions. All computations were performed on a single Intel P4, 1.7 GHz processor with 2.0 GBytes of RAM. For the range of τ values used, a total run time of 1–2 h was required to compute the permeabilities for all 974 throats in the 256^3 subvolume.

We ignore permeabilities computed for the 96 throats whose area is less than 100 μm^2 (equivalent to containing 4 or fewer voxels) as the numerical resolution will be very poor in these cases. In addition, the permeabilities for some throats converged to negative values. In all cases investigated, this resulted when the pore channel contained recirculating flow regimes caused by highly curved channels which result in either the inlet and/or outlet face not being effectively perpendicular to ∇p. Any throats resulting in negative permeability computations were discarded; this left a population of approximately 720 throats (the exact number varying with τ).

Fig. 7 presents the distribution of computed throat permeabilities correlated with throat area of each for the two extreme values of τ used. The scatter in the permeability values of throats of similar area is a reflection of the varied

Table 1
Comparison of residual saturation values

	Image analysis		Bulk measurement	
	s_w	s_o	s_w	s_o
s_{wr}	20%		26–29%	
s_{or}		18%		28–32%
gel		35%		31–34%
gels_{wr}	32%			
gels_{or}		48%		48–50%

geometrical nature of the throat channels. None-the-less, there is a trend to the data (indicated by the least squares fit straight line in each plot) suggesting that a model of the form

$$K = K_1 A^p \tag{6}$$

would provide a working predictor for throat permeabilities that could be used in a network flow model for a Berea core to produce a more realistic simulation. The measured dependence of the parameters p and K_1 as determined from the least square fits to our results is also presented in Fig. 7. The dependence of the permeability results on the value of τ has been observed by others [22,29]. Results by Pan et al. [29] suggest that use of a multiple relaxation time LB can significantly reduce the computed dependence of permeability on the relaxation parameters.

5.3. Fluid characterization

5.3.1. Pore level fluid saturation

Water saturations measured in the imaged region are compared in Table 1 with bulk determinations (on much larger samples) performed in independent experiments

([35]). Our determinations of s_w and s_o at s_{wr} and s_{or} tend to be lower than experimentally measure values, though agreement improves remarkably for gel and gels$_{or}$.

The ability to distinguish individual pores allows the investigation of fluid fractional occupancy (saturation) at the level of individual pores. In Fig. 8(a) we summarize statistics (in the form of box plots [12]) on the distribution of saturations found in pores of different volume ranges. Generally the distributions are skewed, with mean saturation below the 50th percentile at residual fluid conditions. At residual water conditions, it is generally expected that the water (wetting phase) saturation should remain close to one (oil saturation close to zero) in the smaller pores. This is not consistent with our data. Calculation using the Young–Laplace equation however, confirms that oil

should be able to enter the smallest pores visible with our voxel resolution. Specifically, to enter throats of diameter ~5 μm, a capillary pressure around 7 kPa is needed. Thus the 117.2 kPa pressure gradient used is sufficiently strong to mobilize water from the smallest pores detectable with our voxel resolution.

Comparison of the s_{or} and gel plots indicates a surprising increase in oil concentration over most pore sizes in spite of the fact that only aqueous gel has been injected. *This provides both visual and quantitative confirmation of the mobilization of residual oil by the gel from upstream of the imaged region.* Such mobilization has been described previously [45] and is believed to be produced by the injection of the non-Newtonian fluid (gel).
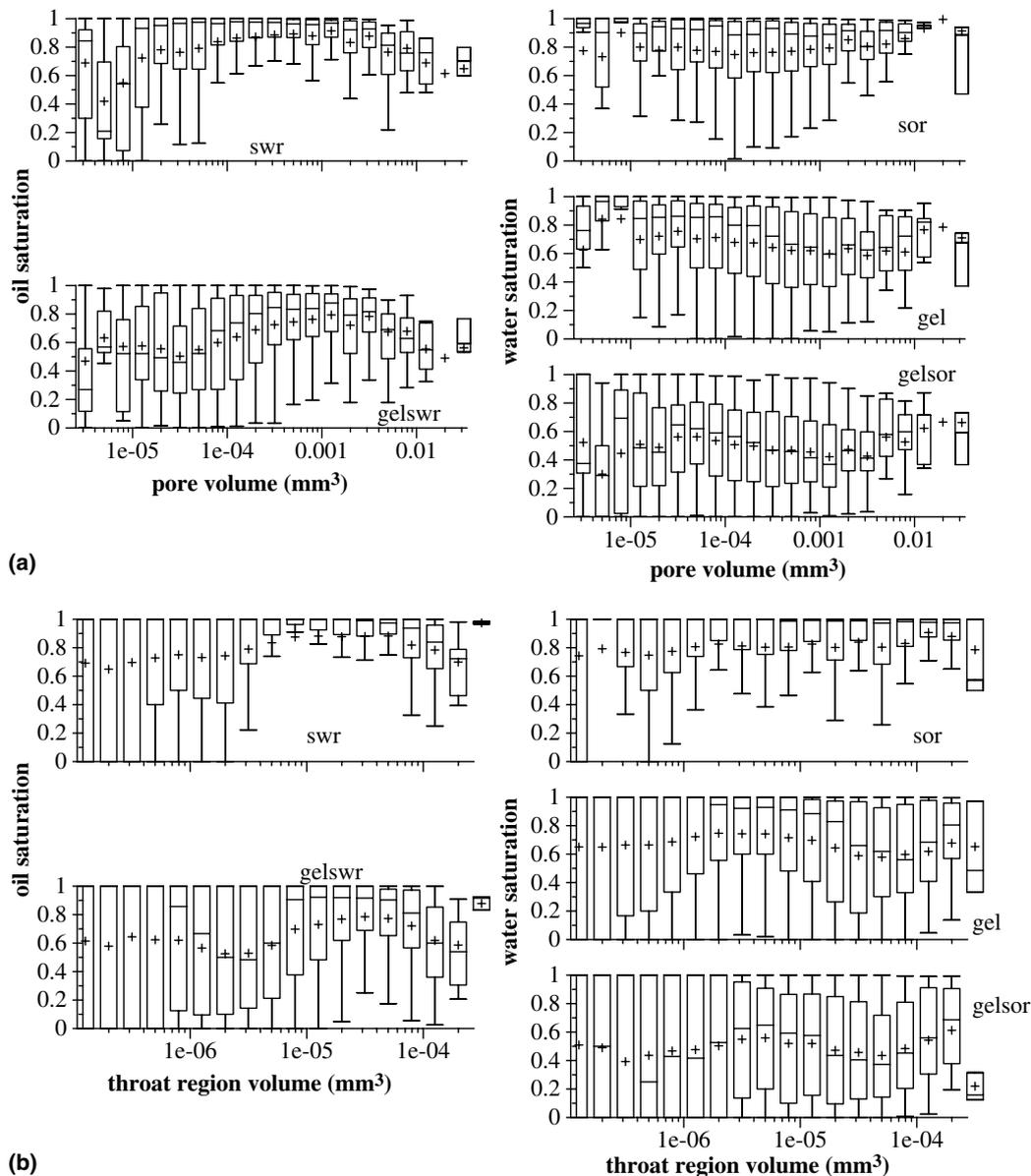

Fig. 8. Distributions of oil saturation (at residual water conditions) and water saturation (at residual oil conditions) as a function of volume for (a) pores and (b) throat regions at the residual fluid conditions investigated. For each volume range, we present a box plot summarizing the distribution of saturations measured in all regions having volume in the specified range.

The effects of the gel on residual fluid distributions can be seen by comparing the s_{wr} distribution with that of $gels_{wr}$ and s_{or} with that of $gels_{or}$. From this comparison it would appear that *gelation effects are not correlated strongly with any specific pore size range.* Fig. 8(b) summarizes saturation statistics only in throat regions. (Specifically a throat region is defined as the set of voxels through which a triangulated throat surface passes.) The plots show no significant difference in behavior in fluid fractionation in throat regions compared to pores, indicating that gelation effects are not correlated strongly with any specific throat size range. *This eliminates gel blocking at throats as a mechanism for disproportionate permeability reduction.* As there is no significant correlation of gelation effects with the pore size, we expect that the same conclusion is valid in the parts of the Berea sample with different porosity.

5.3.2. Fluid connectivity analysis

To further investigate gelation effects, we consider the connectivity of the oil and aqueous phases. Treating the wetting phase (brine) as 26-connected and the non-wetting (oil) as 6-connected, we locate the disconnected "blobs" of each fluid phase. The distribution of blob sizes (expressed as volume) determined for each fluid phase, at each residual fluid condition is presented in Fig. 9.

At s_{wr}, there is a continuum of small brine blob (wetting phase) sizes, the largest of which are less than 0.02 mm^3. The non-wetting phase consists of a single large connected oil blob of volume 1.7 mm^3, and a continuum of small oil blobs of size less than 0.002 mm^3. A similar characterization holds for the fluid distributions in the other 4 images. While it makes sense to refer to the actual volumes of those blobs comprising the continuum spectrum (as these sizes should be determined by the pore size of the rock), the volume of the dominant fluid blob(s) will simply scale with rock volume. We have therefore also displayed the percentage of pore volume occupied by the largest fluid blobs. (These percentages can also be read from the y-axis, though the log-scale makes it difficult.)

In examining Figs. 8 and 9, we caution that conclusions should not be formed on the behavior of the lowest end of the distribution (below 1.2×10^{-6} mm^3, which corresponds to objects of size 10 voxels or less) since misidentification errors between rock and oil voxels would significantly impact results in this region.

As stated, the continuous part of the blob size distribution should be governed by pore size. To demonstrate this, we re-plot the pore volume distribution from Fig. 4, now reporting the total volume occupied by all pores in each size range. To keep Fig. 9 uncluttered, we plot this pore volume distribution only on the middle (gel) plot. *With*
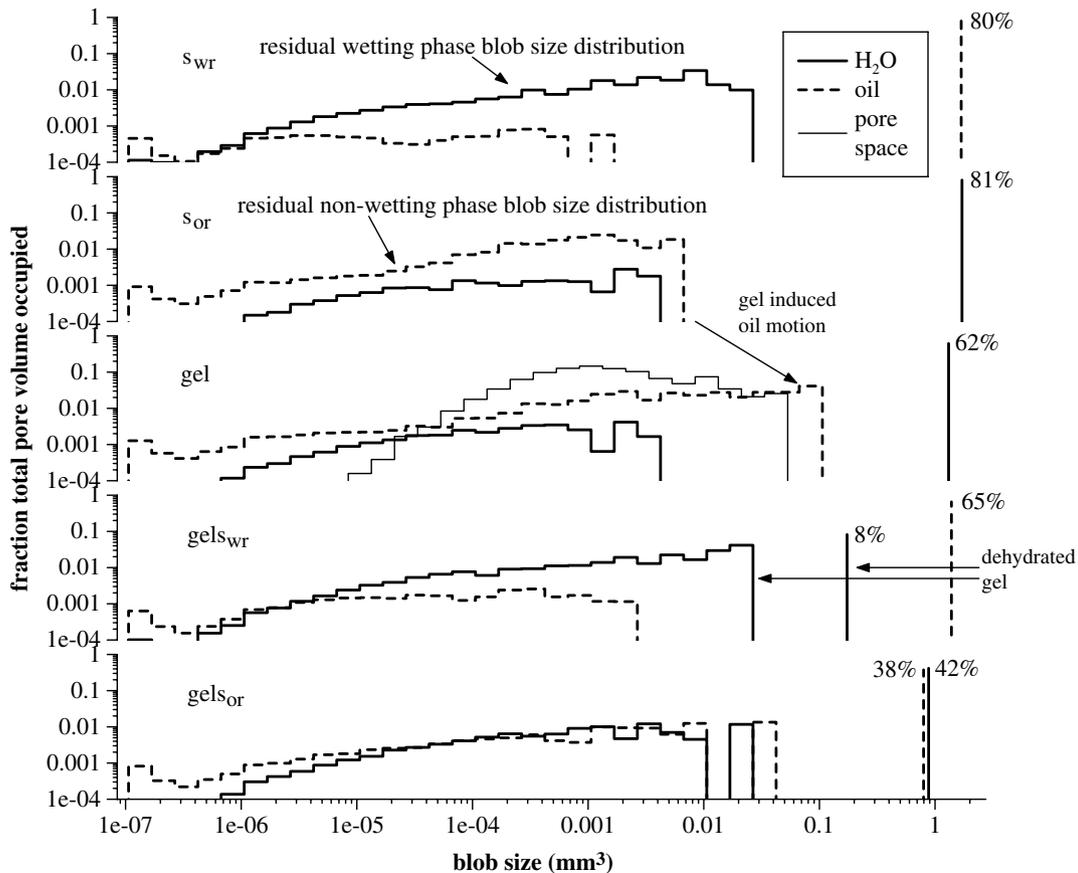

Fig. 9. Distribution of water and oil blob sizes in the images s_{wr} through $gels_{or}$. Blob size (x-axis) is given as a volume. The y-axis displays the total volume (expressed as a fraction of the pore volume) occupied by all blobs in each specified size range.

one exception, the continuum part of the blob size distributions at each residual fluid condition is, in fact, limited by the size of the largest pore. The exception is the continuum spectrum of oil blobs in gel produced, as mentioned above, by mobilization of upstream residual oil due to the introduction of the non-Newtonian gel. During mobilization there is apparently sufficient merging of oil blobs to result in blobs exceeding the size of the largest pores.

In the transition from gel to gels$_{wr}$, oil saturation increased from 35% to 68% (Table 1). As mentioned, the mechanism for this oil displacement and subsequent restoration of an important level of permeability to oil, is germane to field applications. Possibilities for the reduction of gel volume include oil (i) inducing large amounts of mechanical breakage ("ripping") in the linked polymer network; (ii) concentrating (dehydrating) the gel – essentially compressing the polymer network; (iii) mobilizing the gel; and (iv) chemically destroying the gel. As hexadecane is not reactive with any of the gel, brine or rock components, chemical destruction is unlikely. Pressure gradients were closely monitored during floods, and were maintained well below gradients needed to mobilize the gel. In similar, bulk core flood experiments, gel production has never been observed from the core. *Our results support the dehydration mechanism.* Ripping should occur with predominance in large pores, implying oil saturation increases should be greater in large pores. From Fig. 8(a), oil saturation changes from gel to gels$_{wr}$ appear relatively insensitive to pore size. In fact, with a fixed driving pressure gradient, one would expect gel in all pores to be compressed (hydrated) to the same extent.

Effects of gelation are most strongly evident in comparing gels$_{wr}$ with s_{wr}. In gels$_{wr}$ the large residual water blob of volume 0.17 mm^3 (8% PV) and the upper end (above 0.01 mm^3) of the continuum spectrum of water blobs are, we conclude, relatively stationary dehydrated gel blobs. Below 0.01 mm^3, the water blob spectrum of gels$_{wr}$ and s_{wr} are virtually identical, implying these water blobs have

been immobile throughout all fluid flushes and may not have been displaced, even by the gel.

Upon further brine injection (gels$_{or}$, Fig. 9), *we conjecture the gel does not rehydrate significantly* and the pore space is occupied by regions of gel, brine and oil. Some flow paths appear blocked so that a significantly greater fraction of oil becomes trapped. This supports a conjecture that local gel concentration (dehydration) is acting as a blocking mechanism.

To further understand gel behavior, we compare water penetration into two disjoint regions of the pore space. The first region, R_b, occupying 8% PV, is the region occupied by the largest gel blob at gels$_{wr}$ (Fig. 9). The second region, R_o, occupying 65% of the pore volume, is the region occupied by the large oil blob at gels$_{wr}$ (Fig. 9). The percentage volume of each region occupied by water after each stage of flooding is shown in Table 2. From the s_{wr} entry in column 1, we see that R_b is a region of natural high residual water. After gel placement, the residual water (gels$_{wr}$ entry, column 1) content of R_b is doubled. At s_{or} conditions, of course, the water content in R_b is very high, though water injection post-gel (gels$_{or}$ entry, column 1) reduces the water content in R_b by 20%, indicating that some upstream oil does manage to invade some of this gel space.

In contrast, R_o is a region of high oil penetration (entry s_{wr} in column 2) that retains high oil occupancy after gel injection (entry gels$_{wr}$, column 2). From the corresponding entries for s_{or}, gel and gels$_{or}$, we see that *this high oil occupancy is due to a gel enhanced residual oil component that grows from 24% at s_{or} to 62% at gels$_{or}$, indicative of oil trapping.*

5.3.3. Fluid blob characterization

One effect of gel placement is to increase the fluid–fluid surface area for blobs. For a single fluid blob, let a_f denote the area of the blob surface that is in contact with the other fluid phase, and a_r denote the area of the blob surface in contact with rock. Let v_b denote the volume of the blob. Let $\sigma_f \equiv a_f/v_b$ denote the blob's specific fluid surface area and $\sigma_r \equiv a_r/v_b$ denote the blob's specific rock surface area. Table 3 presents the specific surface areas computed for the dominant fluid blobs at each residual condition. At gels$_{or}$, σ_f for the dominant brine blob has increased by a factor of 3 (compared to s_{or}), while σ_f for the dominant (trapped) oil blob has increased by a factor of 2.5 (compared to s_{wr}). Interestingly, σ_r for the dominant oil blob remains approximately constant before and after gel addition (and in good agreement with σ_v, the rock-void specific surface area (first

Table 2
Water saturation in selected regions

	R_b (8% PV)	R_o (65% PV)
s_{wr}	50%	6%
gels$_{wr}$	100%	0%
s_{or}	96%	76%
gel	92%	53%
gels$_{or}$	80%	38%

Table 3
Specific surface areas for pore space and dominant blobs

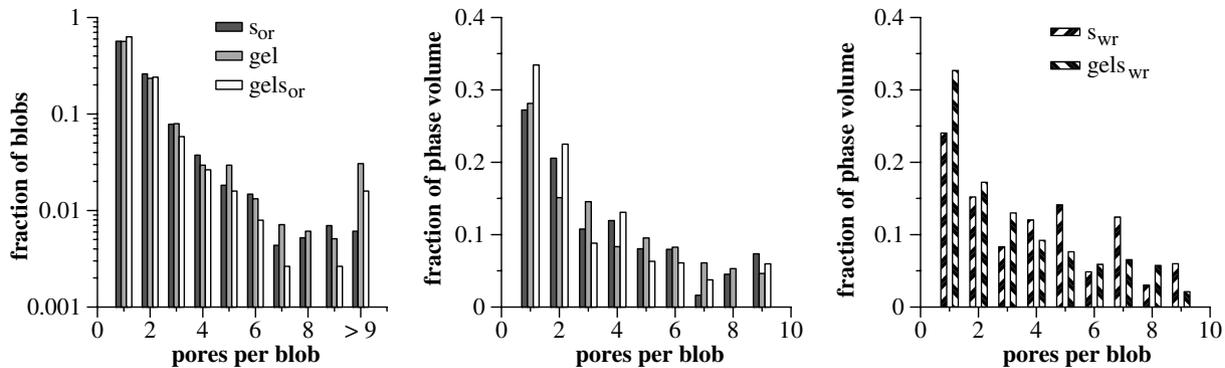|	Pore space	s_{wr}	s_{or}	gel	gels$_{wr}$	gels$_{or}$	
		Oil	Brine	Brine	Oil	Brine	Oil
σ_f (μm^{-1})		0.0165	0.0120	0.0260	0.0253	0.0366	0.0399
σ_r (μm^{-1})	0.0793	0.0802	0.0710	0.0685	0.0754	0.0587	0.0797

Fig. 10. Distribution of blob occupancy.

entry, row 2)), whereas σ_r for the dominant brine blob is always less than σ_v and decreases with gel injection.

In a study on the structure of residual oil saturation, Chatzis et al. [6] reference earlier work [33] on flow in unconsolidated bead packings that found 65% of the oil blobs at residual oil saturation were singlets (i.e. fully contained in single pores), 20% of the blobs were doublets (i.e. spanned two pores), and the rest displayed greater pore occupancy. *Our results confirm and further quantify this observation, though we argue that the results should be phrased in terms of volume fraction, rather than number fraction, of blobs.* On the left of Fig. 10 we plot the observed fraction of oil blobs having various pore occupancy numbers for the images s_{or}, gel and $gels_{or}$. In order to reduce influence of segmentation errors, we ignore all blobs of size smaller than 1.2×10^{-5} mm^3 in producing this plot. The distributions have similar structure, except for a systematic increase in fraction of blobs with large occupancy numbers in gel resulting from upstream oil blob mobilization and merging upon gel injection. We obtain a singlet frequency of 60% and a doublet frequency of 25%. The number frequency distribution however is quite susceptible to changing the imposed cut-off defining small blob size. To remove this dependence, we consider not the fraction of blobs, but the fractional volume of blobs. Consider *all* blobs having occupancy number *only* in the range $1 \rightarrow 9$. Let V_{1-9} denote the total volume occupied by these blobs. Let $V_{1-9}(i)$ denote the total volume occupied by blobs of occupancy i, $i \in [1,9]$. The middle plot in Fig. 10 recasts the occupancy distribution in terms of fractional phase volume $f_V(i) \equiv V_{1-9}(i)/V_{1-9}$. By using fractional volume, and ignoring high occupancy (large volume blobs) we reduce the dependency of the distribution on both segmentation errors and on the presence of any very large oil blobs (as appear in $gels_{or}$) that are not present when gel is absent (s_{or}). Least square fits to a model

$$f_V(i) = f_V(1)i^{-\alpha}, \quad i = 1, \ldots, 9$$

gives consistent values for α of: 0.92 ± 0.26 (s_{or}); 0.78 ± 0.07 (gel); and 0.95 ± 0.16 ($gels_{or}$), and a value of $f_V(1) = 0.31 \pm 0.03$. The quoted errors for α are 1-standard deviation. The right plot in Fig. 10 provides comparison to

the aqueous phase at residual water conditions, s_{wr} and $gels_{wr}$. The distribution of brine blob occupancy at s_{wr} is quite different from the oil case, as is to be expected since brine is the wetting phase, whereas the distribution at $gels_{wr}$ is similar to the oil case. We interpret this to be a reflection of the presence of the polymeric gel which is the overwhelming residual aqueous component at $gels_{wr}$.

Acknowledgements

References

[1] Lindquist WB. 3DMA-Rock, A software package for automated analysis of pore rock structure in 3D computed microtomography images. Available from: http://www.ams.sunysb.edu/~lindquis/3dma/3dma_rock/3dma_rock.html.

[2] Auzerais FM, Dunsmuir J, Ferreol BB, Martys N, Olson J, Ramakrishnan TS, et al. Transport in sandstone: a study based on three dimensional microtomography. Geophys Res Lett 1996;23: 705–8.

[3] Bloomenthal J. Polygonization of implicit surfaces. IEEE Comput Graph Appl 1988;5:341–55.

[4] Blunt MJ. Flow in porous media – pore-network models and multiphase flow. Curr Opin Coll Interface Sci 2001;6:197–207.

[5] Celia MA, Reeves PC, Ferrand LA. Recent advances in pore scale models for multiphase flow in porous media. Rev Geophys 1995;33:1049–57.

[6] Chatzis I, Morrow NR, Lim HT. Magnitude and detailed structure of residual oil saturation. Soc Petrol Eng J 1983;23:311–26.

[7] Chen S, Doolen GD. Lattice Boltzmann method for fluid flows. Ann Rev Fluid Mech 1998;30:329–64.

[8] Dalla E, Hilpert M, Miller CT. Computation of the interfacial area for multi-fluid porous medium systems. J Contam Hydro 2002;56: 25–48.

[9] Deckman HW, Dunsmuir JH, D'Amico KL, Ferguson SR, Flannery BP. Development of quantitative X-ray microtomography. Mater Res Soc Symp Proc 1991;217:97.

[10] Flannery BP, Deckman HW, Roberge WG, D'Amico KL. Three-dimensional X-ray microtomography. Science 1987;237:1439–44.

[11] He XY, Luo LS. Theory of the lattice Boltzmann method: from the Boltzmann equation to the lattice Boltzmann equation. Phys Rev E 1997;56:6811–7.

[12] HyperStat Online Textbook. Available from: http://davidmlane.com/hyperstat/.

[13] Ioannidis MA, Chatzis I, Kwiecien MJ. Computer enhanced core analysis for petrophysical properties. J Can Petrol Tech 1999;38:18–24.

[14] Knackstedt MA, Sheppard AP, Sahimi M. Pore network modelling of two-phase flow in porous rock: the effect of correlated heterogeneity. Adv Water Resour 2001;24:257–77.

[15] Liang Z, Ioannidis MA, Chatzis I. Geometric and topological analysis of three-dimensional porous media: pore space partitioning based on morphological skeletonization. J Colloid Interface Sci 2000;221:13–24.

[16] Lindquist WB, Lee SM, Coker D, Jones K, Spanne P. Medial axis analysis of void structure in three-dimensional tomographic images of porous media. J Geophys Res 1996;101:8297–310.

[17] Lindquist WB, Venkatarangan A. Investigating 3D geometry of porous media from high resolution images. Phys Chem Earth (A) 1999;25:593–9.

[18] Lindquist WB, Venkatarangan A, Dunsmuir J, Wong T-f. Pore and throat size distributions measured from synchrotron X-ray tomographic images of Fontainebleau sandstones. J Geophys Res 2000;105:21508–28.

[19] Lindquist WB. Network flow model studies and 3D pore structure. Contempor Math 2002;295:355–66.

[20] Lindquist WB. Quantitative analysis of three dimensional X-ray tomographic images. In: Bonse U, editor. Developments in X-ray tomography III, Proceedings of SPIE, vol. 4503. Bellingham, WA: SPIE; 2002, p. 103–15.

[21] Lorensen WE, Cline HE. Marching cubes: a high resolution 3-D surface construction. ACM Comput Graph 1987;21:163–9.

[22] Manwart C, Koponen A, Aaltosalmi U, Hilfer R, Timonen J. Lattice-Boltzmann and finite-difference simulations for the permeability of three-dimensional porous media. Phys Rev E 2002;66:016702.

[23] Mason G, Morrow NR. Capillary behaviour of a perfectly wetting liquid in irregular triangular tubes. J Colloid Interface Sci 1991;141(1):262–74.

[24] McKellar M, Wardlaw NC. A method of making two-dimensional glass micromodels of pore systems. J Can Petrol Tech 1982;21:39–41.

[25] Mei R, Luo L-S, Shyy W. An accurate curved boundary treatment in the lattice Boltzmann method. J Comput Phys 1999;155:307–30.

[26] Mei R, Shyy W, Yu D, Luo L-S. Lattice Boltzmann method for 3D flows with curved boundary. J Comput Phys 2000;161:680–99.

[27] Nordhaug HF, Dahle HG, Espedal ME, Gray WG, Celia MA. Two phase flow including interfacial area as a variable. Proc computational methods in water resources, June 25–29, 2000. Rotterdam: Balkema; 2000.

[28] Oh W, Lindquist WB. Image thresholding by indicator kriging. IEEE Trans Pattern Anal Mach Intell 1999;21:590–602.

[29] Pan C, Luo L-S, Miller CT. An evaluation of lattice Boltzmann equation methods for simulating flow through porous media. In: Proc computational methods in water resources, Chapel Hill, NC, June 13–17, 2004.

[30] Patzek TW. Verification of a complete pore network simulator of drainage and imbibition. In: SPE paper #59312 presented at the SPE/DOE improved oil recovery symposium in Tulsa, Oklahoma, 3–5 April 2000.

[31] Radlinski AP, Ioannidis MA, Hinde AL, Hainbuchner M, Baron M, Rauch H, et al. Angstrom-to-millimeter characterization of sedimentary rock microstructure. J Colloid Interface Sci 2004;274:607–12.

[32] Reeves PC, Celia MA. A functional relationship between capillary pressure, saturation and interfacial area as revealed by a pore scale network model. Water Resour Res 1996;32(8):2345–58.

[33] Robinson RL, Haring RE. Experimental study of residual oil configuration in unconsolidated sand. Jersey Prod Res Co Report, Prod Div, Jan 1962.

[34] Seright RS, Liang J-T, Sun H. Gel treatments in production wells with water coning problems. In Situ 1993;17:243–72.

[35] Seright RS, Liang J-T, Lindquist WB, Dunsmuir JH. Characterizing disproportionate permeability reduction using synchrotron X-ray computed microtomography. SPE Reser Eval Eng 2002;5:355–64.

[36] Seright RS, Liang J-T, Lindquist WB, Dunsmuir JH. Use of X-ray computed microtomography to understand why gels reduce permeability to water more than to oil. J Petrol Sci Eng 2003;39:217–30.

[37] Spanne P, Thovert JF, Jacquin CJ, Lindquist WB, Jones KW, Adler PM. Synchrotron computed microtomography of porous media: topology and transports. Phys Rev Lett 1994;73:2001–4.

[38] Succi S. The lattice Boltzmann equation for fluid dynamics and beyond. Oxford: Clarendon Press; 2001.

[39] Talukdar MS, Torsaeter O, Ioannidis MA, Howard JJ. Stochastic reconstruction, 3D characterization and network modeling of chalk. J Petrol Sci Eng 2002;35:1–21.

[40] Thovert JF, Salles J, Adler PM. Computerized characterization of the geometry of real porous-media – their discretization, analysis and interpretation. J Microscopy-Oxford 1993;170:65–79.

[41] Thovert JF, Yousefian F, Spanne P, Jacquin CG, Adler PM. Grain reconstruction of porous media: application to a low-porosity Fontainebleau sandstone. Phys Rev E 2001;63:061307.

[42] Torquato S. Statistical description of microstructures. Ann Rev Mater Res 2002;32:77–111.

[43] Valvatne PH, Blunt MJ. Predictive pore-scale network modeling. In: SPE paper #84550 presented at the SPE annual technical conference and exhibition, Denver (CO), 5–8 October 2003.

[44] Verberg R, Ladd AJC. Simulation of low Reynolds number flow via a time-independent lattice Boltzmann method. Phys Rev E 1999;60:3366–73.

[45] Wang D, Huifen X, Zhongchun L, Qingyan Y. Study of the mechanism of polymer solution with visco-elastic behavior increasing microscopic oil displacement efficiency and the forming of steady "oil thread" flow channels. In: SPE paper #68723 presented at the 2001 SPE Asia pacific oil and gas conference and exhibition, Jakarta, Indonesia, April 17–19, 2001.

[46] Wildenschild D, Hopmans JW, Vaz CMP, Rivers ML, Rikard D, Christensen BSB. Using X-ray computed tomography in hydrology: systems, resolutions, and limitations. J Hydrol 2002;267:285–97.